Metabolic control of type 2 innate lymphoid cells plasticity toward protective type 1-like cells during *Mycobacterium tuberculosis* infection

Dan Corral[1#], Alison Charton[1], Maria Z Krauss[2], Eve Blanquart[3], Florence Levillain[1], Emma Lefrançais[1], Jean-Philippe Girard[1], Gérard Eberl[4], Yannick Poquet[1], Jean-Charles Guéry[3], Rafael J Arguello[5], Matthew R Hepworth[2], Olivier Neyrolles[1,6] and Denis Hudrisier[1,6#]

[1]Institut de Pharmacologie et Biologie Structurale, IPBS, Université de Toulouse, CNRS, UPS, Toulouse, France

[2]Lydia Becker Institute of Immunology and Inflammation, Division of Infection, Immunity and Respiratory Medicine, School of Biological Sciences, Faculty of Biology, Medicine and Health, Manchester Academic Health Science Centre, University of Manchester, Manchester, M13 9PL, UK

[3]Centre de Physiopathologie de Toulouse Purpan (CPTP), Université de Toulouse, INSERM, CNRS, UPS, Toulouse, France

[4]Institut Pasteur, Microenvironment & Immunity Unit, 75724 Paris, France ; INSERM U1224, 75724 Paris, France

[5]Aix Marseille Univ, CNRS, INSERM, CIML, Centre d'Immunologie de Marseille-Luminy, Marseille, France

[6]These authors contributed equally: Olivier Neyrolles, Denis Hudrisier

[#]Corresponding authors: dan.corral@ipbs.fr; denis.hudrisier@ipbs.fr

Abstract

Tissue-resident innate lymphoid cells (ILCs) regulate tissue homeostasis and protect against pathogens at mucosal surfaces and are key players at the interface of innate and adaptive immunity. How ILCs adapt their phenotype and function to environmental cues in their tissue of residence remains to be fully understood. Here we show that *Mycobacterium tuberculosis* infection alters the biology of lung ILCs and, in particular, induces the emergence of a non-classical, protective, interferon-γ-producing ILC1-like population. Adoptive transfer, fate-mapping and *in vitro* differentiation experiments revealed that ILC1-like cells originate from immature ILC2 rather than from mature ILC2. This plasticity is controlled by type 1 cytokines and a glycolytic program involving the transcription factor HIF1α. Collectively, our data reveal how tissue-resident ILCs adapt to their inflammatory and metabolic environment to undergo phenotypic and functional changes toward a pathogen-adapted immune response.

Introduction

Innate lymphoid cells (ILCs) are a population of tissue-resident cells of lymphoid origin that play a key part in both tissue homeostasis and immunity. ILCs are subdivided into three distinct populations based on their expression of cytokines and specific transcription factors. ILC1 depend on T-bet and produce interferon (IFN)-γ, ILC2 depend on GATA3 and produce interleukin (IL)-5 and IL-13, and ILC3 depend on RORγt and produce IL-17A and IL-22[1,2]. Based on these properties, group 1, 2 and 3 ILCs are commonly presented as the innate counterparts of T helper type 1 (Th1), Th2 and Th17 cells, contributing to type 1, 2 and 3 immune responses, respectively.

The regulome of ILCs evolves progressively during the development of each population to reach a state in which key loci relative to that population's specific functions are primed[3]. Yet, several elements controlling cytokine expression or loci encoding lineage-determining transcription factors remain broadly accessible in all ILC subsets[3]. This feature contributes to the remarkable ability of ILCs to dynamically adapt to physiological or pathological alterations in their tissue of residence and to adopt new phenotypic and functional profiles. Thus, the various populations of tissue-resident ILCs can promptly sense and adapt to environmental changes[1, 4] but how they do so only begins to be explored.

In the murine model and in the human pathology of *Mycobacterium tuberculosis* (*Mtb*) infection, prolonged proinflammatory responses are associated with oxidative stress, which favors tissue destruction and triggers a tissue remodeling program. *Mtb* infection is also associated with metabolic changes in the lungs, involving the utilization of aerobic glycolysis primarily instead of oxidative phosphorylation (OXPHOS) in mitochondria (Warburg effect)[5,6]. At the cytokine level, the lungs at steady-state mostly host resting ILC2, which, together with alveolar macrophages, imprint a type 2-oriented environment to the tissue[7,8]. *Mtb* infection of the lung triggers dramatic changes leading to the development of type 1 immunity that is mediated by IFN-γ and associated with protection[9]. While IFN-γ production by $CD4^+$ T lymphocytes in *Mtb* infection[109] has been evidenced for a long time, a recent study in humans provided compelling evidence that other cell types, including ILC1 and ILC2, can contribute to the production of this key cytokine[11].

Here, using the murine model of *Mtb* infection, we explored how lung ILCs respond to chronic pulmonary infection and, in particular, how the major ILC subset in mouse lungs ILC2 adapt to the type 1 inflammation during infection.

Results

ILC1-like cells emerge in the lungs of *Mtb*-infected mice independent of T and B cells

We determined the dynamics and activation of ILC subsets in C57BL/6 mice infected with H37Rv, a laboratory adapted *Mtb* strain. At steady-state, *bona fide* lung ILCs were defined as a population that did not express lineage markers (CD3, CD4, CD8, TCRβ, TCRαδ, CD49b, CD11b, CD11c, B220, CD19, F4/80, GR-1, TER119, FcεR1a) but highly expressed CD90.2 and CD45.2 (Fig. 1a). ILC2, which represent the major ILC population in the mouse lung, were identified after exclusion of ILC1 (NK1.1$^+$) and ILC3 (RORγt$^+$) cells. We observed significant heterogeneity among ILC2 at steady-state, with a subset expressing IL-18Rα that expressed ILC2 markers GATA3, ST2, Arg1, and IL-5 at lower levels than in ILC2 cells not expressing IL-18Rα (Fig. 1a and Supplementary Fig. 1a-d). Strikingly, during *Mtb* infection, IL-18Rα-expressing ILC2 markedly increased and, importantly, an ILC population expressing both IL-18Rα and T-bet emerged (Fig. 1a).

Further phenotypical analysis revealed that the ILC subset co-expressing IL-18Rα and T-bet displayed little to no classical ILC2 markers GATA3, ST2, Arg1 and IL-5 (Fig. 1a, b and Supplementary Fig. 1e-g) or the ILC3 marker IL-17A (Fig. 1a and c). Like ILC1, this subset expressed T-bet, CD49a and CD226 and produced IFN-γ (Fig. 1a and d; Supplementary Fig. h-j). However, unlike ILC1 or NK cells, these cells did not express NK1.1 (gated on NK1.1 negative ILCs), NKp46 or Eomes (Fig. 1a and Supplementary Fig. 1k). We therefore named this new subset as ILC1-like cells. In order to better decipher the heterogeneity of ILCs during *Mtb* infection, we used an unsupervised flow cytometry approach. This allowed us to clearly identify the expected presence and abundance of typical ILC subsets in uninfected animals and, more importantly, the emergence of the ILC1-like subset during *Mtb* infection (Fig. 1e).

While ILC1, ILC3, and IL-18Rα$^+$ ILC2 increased following a similar kinetic upon *Mtb* infection (Fig. 1f, g, h), IL-18Rα$^-$ ILC2 progressively decreased (Fig. 1i). ILC1-like cells became detectable after 21 days of infection and dramatically expanded in the following weeks (Fig. 1j). The dynamics of these ILC populations was well reflected by their index of proliferation, as revealed by Ki-67 staining (Supplementary Fig. 1l). Interestingly, the emergence of ILC1-like cells was conserved in the C3HeB/FeJ mouse, which is more sensitive to *Mtb*, both phenotypically and functionally (Supplementary Fig. 1m-n).

Since the adaptive immune cells reach the site of infection starting from day 21 post-*Mtb* infection[12] and therefore coincides with the detection of ILC1-like cells, we determined if these two processes were linked. Interestingly, *Rag2*$^{-/-}$ mice lacking the adaptive immunity presented an enhanced generation of ILC1-like cells compared to wild-type mice, demonstrating that adaptive immunity is not necessary for the generation of ILC1-like cells (Supplementary Fig. 1o).

Altogether, our data show that in the lung during *Mtb* infection, classical ILC1 and ILC3 expand, IL-18Rα$^-$ ILC2 contract and, most notably, a previously unidentified ILC1-like cell population emerges, which contributes to IFN-γ production.

Pulmonary ILC2 give rise to ILC1-like cells during *Mtb* infection

ILCs have been reported to adapt their profile to environmental cues and ILCs with characteristics of ILC1-like cells have been shown to emerge from various origins[13, 14]. Because we show, for the first time, the emergence of ILC1-like cells in the context of *Mtb* infection and that ILC1-like cells were undetectable before the infection, we hypothesized that ILC1-like cells could arise from pre-existing lung ILC2. To test this hypothesis, we adoptively transferred total lung ILC2 purified based on ST2 positivity regardless of their IL-18Rα expression into *Rag2*$^{-/-}$*Il2rg*$^{-/-}$ mice, which are devoid of T cells, B cells, and NK/ILCs, one day before *Mtb* infection (Supplementary Fig. 2a and b). Before transfer, we confirmed that purified ILC2 expressed GATA3 but not T-bet or RORγt (Supplementary Fig. 2c) and noted that IL-18Rα expression was lost during *in vitro* culture (Supplementary Fig. 2c). Confirming our hypothesis, transferred ILC2

strongly upregulated T-bet in infected, but not in non-infected, mice (Fig. 2a, b). Furthermore, based on Ki67, T-bet^{high} cells represented the most proliferative population among ILC2 (Fig. 2c). Importantly, higher amounts of IFN-γ were detected in the lung of infected *Rag2*$^{-/-}$*Il2rg*$^{-/-}$ mice after ILC2 transfer (Fig. 2d), suggesting that ILC1-like cells generated from ILC2 contribute to IFN-γ production.

Next, we determined if ILC1-like cells derive from mature, IL-5-producing, ILC2. For this, we crossed IL-5$^{Cre\text{-}tdTomato}$ (Red5) mice with ROSA26-YFP mice to enable fate-mapping mature ILC2[15] and confirmed that IL-5 was selectively expressed by ST2^{+} ILC2 but not by IL-18Rα^{+} ILC at steady-state (Supplementary Fig. 2d). Surprisingly, very few IL-18Rα^{+} ILC2 and ILC1-like cells expressed IL-5 and YFP after *Mtb* infection, compared to IL-18Rα^{-} ILC2 (Fig. 2e, f). These results demonstrate for the first time that mature ILC2 are not a major source for generating ILC1-like cells. In agreement with this result, using a model of T-bet deficiency in IL-5^{+} cells (IL-5^{Cre}Tbx21$^{fl/fl}$ mice), we found that ILC1-like cells remained present in spite of the absence of T-bet expression in mature ILC2 (Supplementary Fig. 2e, f). Based on this set of results, we therefore anticipated that ILC1-like cells most likely derived from immature ILC2.

We (Fig. 1 and Supplementary Fig. 1) and others[16,17] reported the presence of a discrete subset of IL-18Rα^{+} ILC2 at steady-state harboring a less activated phenotype compared to IL-18Rα^{-} ILC2 and ILC2 precursor (ILC2P). To assess if immature ILC2, such as ILC2P from BM, have the potential to give rise to ILC1-like cells, we performed an *in vitro* differentiation assay in the presence of type 1 or type 2 activating cytokines. Because of the low numbers of ILC2P in the lungs, we purified them from the bone marrow. We found that ILC2P acquired T-bet and IFN-γ expression, showing their ability to engage in ILC1-like differentiation, only in the presence of type 1 cytokines (Fig. 2g-j). In addition, we showed that the IL-18Rα^{+} ILC2 subset, unlike the IL-18Rα^{-} ILC2 subset, shares similarities with bone marrow ILC2P, including the expression of TCF-1 and PLZF, thus suggesting that this lung-resident subset forms a population of immature ILC2 (Fig. 2k, l). Together, our results strongly suggest that immature rather than mature ILC2 give rise to ILC1-like cells during *Mtb* infection.

Type 1 and type 2 inflammation govern the generation of ILC1-like and mature ILC2, respectively

Mtb infection triggers the development of type 1 immunity [9] in the lung, which is largely imprinted with a type 2 environment [7,8]. Therefore, we next investigated the impact of type 1 and type 2 cytokines on the generation of ILC1-like cells. IL-12 is a well-known cytokine initiating IFN-γ production by ILC1 and NK[18,19], which is potentiated in the presence of IL-18[18,19]. Moreover, IL-18 complements IL-12's action to establish a type 1 inflammatory environment during *Mtb* infection [9,20]. We administered mice with IL-12 ± IL-18 intranasally for 1 week and found a decreased ILC2 function, such as IL-5 production (Supplementary Fig 3a-c), in both mature and immature ILC2 as well as an induced IFN-γ production in immature ILC2 (Supplementary Fig. 3c). Remarkably, administration of both IL-12 and IL-18 was sufficient to induce the generation of IFN-γ -producing ILC1-like cells in the lungs (Fig. 3a-c). Thus, we could closely recapitulate the generation of ILC1-like cells observed during *Mtb* infection with the simple administration of IL-12 and IL-18. IFN-γ is well-known to repress ILC2 function[21,22], we therefore determined its role in the generation of ILC1-like cells. IL-12+IL-18 administration led to a 3-fold reduction in the differentiation of ILC1-like cells in *Stat1*$^{-/-}$ mice, which cannot signal through type 1 and type 2 IFN, compared to in wild type mice (Fig. 3d, e). Similar results were obtained upon blocking IFN-γ in WT mice (Fig. 3f). These results demonstrated a critical role played by IFN-γ in driving ILC1-like differentiation.

IL-33, a well-known inducer of both mature and immature ILC2, had no impact on the generation of ILC1-like cells but promoted their generation when combined with IL12 and IL-18 (Fig. 3g and Supplementary Fig 3a). IL-33 alone clearly induced high numbers of IL-18Rα^{+} ILC2 (Fig. 3g and Supplementary Fig 3a) but these cells expressed IFN-γ only when IL-12+IL-18 were added (Supplementary Fig. 3a-d). Interestingly, the combination of IL-12, IL-18, and IL-33 induced a mixed ILC1 and ILC2 phenotype characterized by the expression of both IL-5 and IFN-γ (Supplementary Fig. 3a-d). Because ST2 is expressed by various cell types, including ILC2, we also tested Neuromedin U (NMU), whose receptor is solely present in bone marrow ILC2P and in lung ILC2[23–25]. Similar to IL-33, NMU potentiated the generation of ILC1-like cells induced by IL-12 and IL-18 (Fig. 3h).

These results strongly suggest that IL-18Rα^{+} ILC2 represent a highly adaptable subset that retains the potential to differentiate into mature ILC2 or ILC1-like cells in

response to type 2 or type 1 cytokines, respectively, depending on the inflammatory context.

Metabolic environment dictates ILC2 plasticity through glucose availability

Metabolism and metabolic reprogramming are key events in the development and function as well as the adaptation to environmental cues of ILCs [26]. *Mtb* infection is associated with inducing a Warburg effect in the lungs [5,6]. This observation prompted us to explore if glycolysis impact on the cellular changes affecting ILC we report here.

To test this hypothesis, we first treated mice with 2-deoxyglucose (2-DG), a glycolysis inhibitor, during *Mtb* infection (Fig. 4a). 2-DG administration marked decreased both the percentage and the number of ILC1-like cells as well as diminished the ability of ILC1-like cells to produce IFN-γ (Fig. 4b and c). Next, since glucose is consumed in the lungs of *Mtb*-infected mice[6], we investigated if the modulation of glucose availability in the lung environment could modulate ILC2 plasticity (Fig. 4d). Glucose supplementation in the animals' drinking water greatly enhanced the differentiation of ILC1-like cells (Fig. 4e) and augmented the percentage of IFN-γ$^+$ ILC1-like cells (Fig. 4f). Interestingly, 2-DG or glucose supplementation had little to no impact on other ILC subsets and their production of IFN-γ (Supplementary Fig. 4a-b). There was a trend toward a decrease in NK cells upon 2-DG treatment and a greater ability of these cells to produce IFN-γ upon glucose supplementation (Supplementary Fig. 4c-f). Altogether, these results supported the hypothesis that the metabolic environment controls ILC2 plasticity.

Arg1 was previously identified as a critical component of the metabolic programming of lung ILC2, with its inhibition or genetic inactivation resulting in reduced aerobic glycolysis[27]. Arg1 was highly expressed in both mature and immature ILC2 but not in ILC1-like cells generated after *Mtb* infection or cytokine administration (Fig. 5a), which prompted us to explore in more details the metabolic status of the ILC1-like cells. To do this, we took advantage of the recently described SCENITH method[28], which allows to functionally determine global metabolic dependencies and capacities at the single cell level. SCENITH uses protein synthesis levels as a readout and is particularly appropriate to analyze the metabolism of rare cells, such as ILCs. ILC1-like cells were compared to control cells known to rely on a glycolytic metabolism (*e.g.* NK cells) and to ILC2. IL-12+IL-18 administration increased and reduced protein synthesis levels in

NK cells and ILC2, respectively, as estimated by the staining for and the amount of incorporated puromycin (Fig. 5b and c). ILC1-like cells presented the highest levels of protein synthesis among all cells tested. These results are in accordance with the activation status of these cells (Fig. 3). In addition, the analysis of protein synthesis in the presence of inhibitors targeting different metabolic pathways allowed us to assess glucose dependence, mitochondrial dependence and glycolytic capacity of the cell types of interest (Fig. 5d-g). While IL-12+IL-18 administration did not affect the glucose dependence of NK cells and ILC2 (Fig. 5e), it diminished mitochondrial dependence while increased glycolytic capacity (Fig. 5f,g), a typical feature of the Warburg effect[29]. The strong metabolic activity of ILC1-like cells (Fig. 5b,c) relied on the glycolytic pathway similar to NK cells and ILC2 in IL12+IL-18 treated mice (Fig. 5e-g). Surprisingly, the metabolic status of IL18Rα^+ ILC2 did not change upon IL-12+IL-18 treatment, and therefore differed from that of NK and ILC1-like cells (Fig. 5e-g). Finally, inhibition of glycolysis during *ex vivo* stimulation of total lung ILCs decreased IFN-γ^+ ILCs (Fig. 5h), showing that IFN-γ production is glycolysis-dependent.

These results demonstrate that while the metabolic reprograming towards glycolysis is observed in NK, ILC2 and ILC1-like cells, this metabolic profile is a hallmark of activation for NK and ILC1-like cells and of inhibition for ILC2.

Metabolic reprogramming involving HIF1α controls ILC2 plasticity

Several studies suggested that the Warburg effect, a metabolic pathway that is at work during *Mtb* infection[5,6], relied on the transcription factor hypoxia-inducible factor-1 α (HIF1α) in a different context [30]. Interestingly, it was shown in a model of von Hippel-Lindau (VHL) deficiency, where HIF1α is overexpressed, that ILC2 development was repressed through glycolysis induction[31]. IL-12+IL-18 administration resulted in the activation of ILC1-like cells and the inhibition of ILC2 (Fig. 3) and induced the glycolytic pathway (Fig. 5). This prompted us to investigate the involvement of HIF1α in ILC2 plasticity toward ILC1-like.

HIF1α is regulated at both transcriptional and post-translational levels with O_2-dependent and -independent mechanisms[30]. Because of technical limitations imposed

by the time necessary to process lungs in Biosafety Level 3 facility as well as by the number of cells accessible, we could not use antibody-based approaches to measure the HIF1α protein. Therefore, we measured the *Hif1a* mRNA level by flow cytometry in non-infected *vs*. *Mtb*-infected mice. While *Hif1a* mRNA was poorly expressed in mature ILC2 and NK cells in non-infected mice, its expression was strongly upregulated in these cells during *Mtb* infection (Fig. 6a). In addition, *Hif1a* mRNA was expressed by ILC1-like cells both at the expression level (Fig. 6a, left graph) and in the percentages of expressing cells (Fig. 6a, right graph) compared to mature ILC2 from *Mtb*-infected mice (Fig. 6a). Using this approach, we also confirmed that IFN-γ was well-induced in NK cells and highly expressed by ILC1-like cells but was undetectable in ILC2 (Fig. 6b). Comparison of ILC1-like cells to mature and immature ILC2 during *Mtb* infection showed that different percentages of these cells expressed *Il5* and *Ifng* mRNA (Fig. 6c-d), confirming the results of IL-5 and IFN-γ proteins (Fig. 1). The percentages of cells expressing *Hif1a* mRNA was high and with no substantial differences among these three cell subsets (Fig. 6e). Interestingly, the profile of *Ifng*, *Il5* and *Hif1a* mRNA expression in ILC1-like cells and in mature and immature ILC2 in mice administered with IL-12+IL-18 was similar to that in *Mtb*-infected animals (Supplementary Fig. 5a-c), revealing that type 1 inflammation, including that induced by *Mtb* infection, drives HIF1α expression in lung resident ILCs. Noteworthy, the expression of *Ifng* mRNA was concomitant with *Hif1a* mRNA expression (Supplementary Fig. 5d). Moreover, the generation of mitochondrial ROS (mtROS), an event tightly linked to HIF1α-expression[32], was markedly upregulated in ILC1-like cells (Supplementary Fig. 5e), suggesting that HIF1α protein could be differentially expressed between ILC1-like cells and ILC2 although these subsets display comparable *Hif1a* mRNA levels. These results support the notion that HIF1α is well-induced in ILC2 and ILC1-like cells, suggesting that HIF1α might participate in ILC1-like differentiation through sustaining glycolysis induction.

To further explore this hypothesis, we performed an *in vitro* assay using purified ILC2 cultured in the presence of DMOG, which induces the stabilization of the HIF1α protein[30] (Fig. 6f). DMOG-treated ILC2 reduced the expression of ILC2 markers GATA3 and ST2 (Fig. 6g). Impressively, DMOG treatment alone was sufficient to upregulate genes typically associated with an ILC1 phenotype, such as *Tbx21*, *Ifng* and *Il18r1* (Fig. 6h). At the transcriptional level, DMOG treatment induced the

upregulation of genes implicated in the glycolytic pathway (Supplementary Fig. 5f). Accordingly, analysis of the global metabolic profile of ILC2 revealed that DMOG-treated ILC2 harbored a glycolytic profile, while untreated ILC2 rather use mitochondrial respiration (Fig. 6i-l).

Altogether, these results demonstrate that induction of HIF1α in lung ILC2 connects glycolysis induction with the inhibition of their phenotype, which reminisces the observation made in our *in vivo* models (Fig 1, 3, and 5), and favors, at the same time, the acquisition of an ILC1-like profile.

ILC1-like cells confer protection against *Mtb*

Next, we investigated whether BCG, the only available vaccine for TB, might impact the population of lung-resident ILCs when delivered intranasally, a route providing a better protection than the conventional subcutaneous route[33], prior to *Mtb* infection. As expected, mucosal BCG vaccination induced protection upon *Mtb* challenge (Fig. 7a). In vaccinated mice, protection correlated with an increase in T-bet expression in ILCs (Fig. 7b). More importantly, although BCG vaccination had no impact on other ILC subsets (Fig. 7c-g), higher numbers of ILC1-like cells were detected at 14 days post-infection, a time when IFN-γ -producing ILC1-like cells were virtually absent from non-vaccinated mice (Fig. 7e, h, i as well as Fig 1) but well-induced in vaccinated mice (Fig. 7e, h, i). Overall, BCG vaccination promotes ILC1-like cells in early stages of infection, which could contribute to protection against *Mtb*.

We then addressed the protective role of ILC2 and ILC1-like cells against *Mtb* using an adoptive transfer model. Transfer of purified lung ILC2 expanded *in vitro* did not lead to a reduction in bacterial loads compared to non-transferred mice when analyzed at 14 days post-infection. In sharp contrast, a statistically significant reduction in bacterial load was observed in ILC2-transferred mice above control mice when analyzed at day 21 post-infection (Fig. 7j). Interestingly, the increase in T-bet expression was only observed after day 21, and not after day 14, strongly suggesting that protection was rather due to ILC2 engaged in plasticity (Fig. 7k).

316 Finally, to assess the contribution of ILC2 plasticity to protection against *Mtb*, we
317 took advantage of the cytokine-based plasticity model (Fig. 2) to generate sufficient
318 numbers of ILC1-like cells for adoptive transfer. Remarkably, the transfer of as few as
319 10,000 ILC1-like cells resulted in a statistically significant reduction in bacterial load,
320 demonstrating for the first time the protective capacity of ILC1-like cells against the TB
321 bacillus (Fig. 7l).

Discussion

Here, we examined how *Mtb* infection impacts the biology of lung-resident ILCs in the mouse model. We report that lung ILCs exhibit dramatic changes upon *Mtb* infection, with ILC1 and ILC3 showing progressive expansion while mature ILC2, the main ILC population in the lung, undergo contraction. Unexpectedly, an immature subpopulation of ILC2 expressing IL-18Rα present in very low proportion at the steady state progressively expand during infection. Even more strikingly, *Mtb* infection results in the appearance of an ILC2 population exhibiting characteristics of ILC1 (ILC1-like cells). Using a non-infection cytokine-dependent model, we found that immature ILC2 sense and adapt to their environment to strengthen the ILC2 response in a type 2 environment (administration of IL-33 or NMU) or to differentiate into IFN-γ-producing ILC1-like cells in a type 1 environment (administration of IL-12 and IL-18). Importantly, we found that type 1 immunity induces a glycolytic signature in both ILC2 and ILC1-like cells but results in their inhibition and activation, respectively. Inhibition of glycolysis or glucose supplementation *in vivo* revealed that both the generation and function of ILC1-like cells critically depend on their metabolic environment. Furthermore, stabilization of HIF1a in ILC2 is sufficient to trigger an ILC1-like signature in these cells, suggesting a key role for HIF1a in ILC2-to-ILC1-like cell transition. Finally, we report that ILC1-like cells are induced after BCG vaccination and exhibit a protective potential against *Mtb* infection.

Recently, ILC3 were reported to mediate protection against *Mtb* through induction of lung ectopic lymphoid follicles[34]. Although our results confirm the expansion and activation of ILC3 during *Mtb* infection, our study reveals a more global alteration of the ILC compartment in this context, including both ILC1 and ILC2. In particular, and for the first time during *Mtb* infection, we report the plastic differentiation of ILC2, the most prominent ILC subset in the mouse lung[2,35], toward ILC1-like cells. Differences between the two studies may be due to the strains of *Mtb* used (HN878[34] *vs.* H37Rv in our study), the markedly different proportions of the various ILC subsets in the lungs reported in the two cases, or both.

Based on adoptive transfer experiments as well as on the ability of NMU to promote ILC1-like cells, we found that ILC1-like cells appearing during *Mtb* infection originate from an ILC2 population. While the plastic differentiation of lung ILC2 to ILC1-like cells

has previously been reported in the influenza virus infection model, whether they originate form mature or immature ILC2 was not addressed [14]. We now demonstrate that mature (IL-5 producing) ILC2 display a very limited potential to differentiate into ILC1-like cells as evidenced using a fate-mapping approach. As described in recent reports[4,17], lung ILC2 is a complex and heterogeneous population of cells with a broad spectrum of maturity. Although the identity of the immature ILC2 population giving rise to ILC1-like cells remains to be formally demonstrated, we identified an immature ILC2 subset, based on the expression of IL-18Rα, sharing phenotypic similarities with bone marrow ILC2P, which retains the ability to differentiate into ILC1-like cells. These results raise the exciting possibility that local precursors formed by immature ILC2 may undergo an *ILCpoiesis*[16,17] controlled by the inflammatory context that may drive the generation of ILC subsets adapted to *Mtb* infection in the lungs, as suggest in human ILC biology[36,37]. In this regard, type 1 or type 2 environments triggered by cytokines drove the conversion of IL-18Rα$^+$ ILC2 toward mature ILC2 or ILC1-like cells, respectively. Although the potential of immature ILC2 to generate various ILC populations was demonstrated *in vitro*, to our knowledge, our report is the first to show the generation of ILC1-like cells from immature ILC2 *in vivo* in a relevant pathophysiological setting.

The impact of infection-induced metabolic reprogramming on the phenotype of immune cells represents a field of intense investigation, which remains particularly focused on abundant cells, such as T lymphocytes and macrophages. In contrast, little is known regarding how less abundant tissue-resident cells, such as ILCs, adapt to their environment during infection to trigger an appropriate response[26]. Since *Mtb* infection triggers major environmental changes[5,6], we questioned how metabolism contributes to the plastic differentiation of ILC1-like cells.

We report for the first time that newly generated ILC1-like cells critically depend on glycolytic metabolism that is independent of Arg1. Interestingly, glycolytic pathway is also induced in ILC2, but in this case, it is rather associated with their inhibition. In this case, Arg1, which is constitutively expressed by lung and bone marrow ILC2[27,38], was linked to the ability of ILC2 to perform glycolysis and to sustain their functions[27]. However, the induction of HIF1α during ILC2 development in VHL-deficient mice unfavored the acquisition of an ILC2 phenotype through metabolic and epigenetic

386 regulation[31]. Taken together, these results suggest that cells with a dramatically
387 different fate such as ILC2 and ILC1-like cells may rely on the same global metabolic
388 pathway. In fact, it seems that the association of metabolic machinery and metabolite
389 availability in tissues reflect the fate of ILC2 *vs.* ILC1-like cells. Indeed, we observed
390 that during type 1 inflammation, both ILC2 and ILC1-like cells express HIF1α but
391 stabilization of HIF1α in ILC2 favors an ILC1-like signature rather than stabilizing their
392 phenotype. Our results support the notion that HIF1α contributes to glycolysis
393 induction in both ILC2 and ILC1-like cells and in the generation and function of the
394 latter cell type. Glycolysis has been tightly connected to the production of IFN-γ by
395 various means such as epigenetic modification and post-transcriptional regulation of
396 *Ifng* mRNA[39,40]. In accordance, we report that DMOG-mediated stabilization of the
397 HIF1α protein in ILC2 *in vitro* favors both glycolysis induction and *Ifng* mRNA
398 expression. We found that *in vivo Ifng* mRNA was highly expressed in ILC1-like cells
399 and correlated with high *Hif1a* mRNA expression in these cells. While the HIF1α
400 protein expression could not be directly addressed *in vivo*, these results strongly
401 suggest that the HIF1α protein is stabilized in ILC1-like cells and is implicated in
402 glycolysis induction and, subsequently, IFN-γ production. Different levels of mtROS
403 found in IL-18Rα$^-$ ILC2, IL-18Rα$^+$ ILC2, and ILC1-like cells corroborate this hypothesis.
404 Supporting this notion, *ex vivo* stimulation of ILC1-like cells in the presence of a
405 glycolysis inhibitor blocks IFN-γ production by these cells.

406 Collectively our results highlight the role played by environmental changes imposed
407 by inflammatory and/or metabolic programs on the fate and function of tissue-resident
408 ILCs. Future studies will aim at understanding the intrinsic and extrinsic molecular
409 mechanisms at play during this process. Our observation that BCG vaccination favors
410 the early generation of ILC1-like cells and that ILC1-like cell are endowed with a
411 protective potential during *Mtb* infection pave the way for future studies aiming at
412 elucidating the role played by ILC1-like cells in protection. On a broader perspective,
413 targeting ILC1-like cells using dedicated strategies may help develop novel
414 approaches to influence pathological situations where their emergence is favored.

415

Materials & Methods

Mice

Six-to-eight-week-old female C57BL/6 mice were purchased from Charles River Laboratories France (Saint Germain Nuelles, France). *Rag2*$^{-/-}$ (B6.129-Rag2tm1Fwa), *Rag2*$^{-/-}$*Il2rg*$^{-/-}$ (C;129S4-Rag2tm1.1Flv Il2rgtm1.1Flv/J), Red5 mice (B6(C)-Il5tm1.1(icre)Lky/J)n, *Stat1*$^{-/-}$ (B6.129S(Cg)-Stat1tm1Dlv/J) and *Tbx21*$^{flox/flox}$ (B6.129-Tbx21tm2Srnr/J) mice on a C57BL/6 J were bred in our animal facility. C3HeB/FeJ, and ROSA26-YFP mice (B6.129X1-*Gt(ROSA)26Sor*$^{tm1(EYFP)Cos}$/J; 006148) were purchased from The Jackson Laboratory through Charles Rivers Laboratory France. All mice were maintained in specific-pathogen-free animal facility at IPBS and all experiments were conducted in strict accordance with French laws and regulations in compliance with the European Community council directive 68/609/EEC guidelines and its implementation in France under procedures approved by the French Ministry of Research and the FRBT (C2EA-01) animal care committee (APAFIS #1269, #3873, #10546, #16529 and #17384).

Mtb culture, immunization & mouse infections

The laboratory strain of *Mtb*, H37Rv, was grown at 37°C in Middlebrook 7H9 medium (Difco) supplemented with 10% albumin-dextrose-catalase (ADC, Difco) and 0.05% Tyloxapol (Sigma), or on Middlebrook 7H11 agar medium (Difco) supplemented with 10% oleic acid-albumin-dextrose-catalase (OADC, Difco). Six- to eight-week-old mice were anesthetized with a cocktail of ketamine (60 mg/kg, Merial) and xylasine (10 mg/kg, Bayer) and infected intranasally (i.n.) with 1000 CFUs of mycobacteria in 25 µL of PBS containing 0.01% Tween 80. For immunization, C57BL/B6 mice were immunized i.n. with 5.10^5 CFU of BCG (Danish), and were challenged 60 days post-vaccination with H37Rv as previously described[33]. All experiments using *Mtb* were performed in appropriate biosafety level 3 (BSL3) laboratory and animal facility.

In vivo treatments

Mice were injected intraperitoneally (i.p) one day before infection with either 100 µg of mAb to NK1.1 (PK136, BioXcell) or 200 µg of mAb to IFNγ (BioXcell) or its isotype control and the procedure was repeated twice a week until completion of the experiment and sacrifice of the mice. 2-DG (1g/kg, Sigma) was injected every other day starting from the day of infection and until completion of the experiment. For glucose supplementation, mice were treated with drinking water containing 30% (w/v) glucose (started 1 week before infection until sacrifice).

Adoptive transfer experiments

For the adoptive transfer of ILCs, *in vitro* cultured ILC2 were harvested after 7 days of culture and $5x10^5$ to $2x10^6$ cells were transferred i.v. in mice anesthetized with isoflurane one day before *Mtb* infection in *Rag2*$^{-/-}$*Il2rg*$^{-/-}$. For ILC1-like transfer, $1x10^4$ purified ILC1-like were directly transferred via intratracheal (i.t.) route in mice anesthetized with isoflurane one day before *Mtb* infection in *Rag2*$^{-/-}$*Il2rg*$^{-/-}$.

Lung harvest

Mice were sacrificed any cervical dislocation under isoflurane anesthesia and lungs were harvested aseptically, homogenized using a gentleMACS dissociator (C Tubes, Miltenyi) in HBSS (Difco), and incubated with DNAse I (0.1 mg/mL, Roche) and collagenase D (2 mg/mL, Roche) during 30 min at 37°C under 5% CO2. When indicated, mice received an i.v. injection of labeled anti-CD45 mAb (5µg) 5 minutes before sacrifice to discriminate between parenchymal and intravascular cells in subsequent flow cytometry analyses. Lungs homogenates were filtered on 40 µm cell strainers and centrifuged at 329 × g during 5 min. Supernatants were conserved for cytokine content analysis. A part of the cellular pellet was conserved in TRIzol reagent for cellular RNA analysis. Bacterial loads (colony forming units) were determined by plating serial dilutions of the lung homogenates onto 7H10 solid medium (Difco) supplemented with 10% oleic acid-albumin-dextrose-catalase (OADC, Difco). The plates were incubated at 37°C for 3 weeks before bacterial CFUs scoring. In the remaining fraction, red blood cells were lysed in 150 mM NH4Cl, 10 mM $KHCO_3$, 0.1 mM EDTA (pH 7.2) for immunological staining.

In situ expansion of ILC

To expand ILC2, C57BL/6 or *Rag2*$^{-/-}$ mice were treated intranasally (i.n.) with 100 ng of recombinant IL-33 (Biolegend) each day for 5 consecutive days. For the cytokine-based plasticity model, C57BL/6 or *Rag2*$^{-/-}$ mice were treated i.n. with different combinations of cytokines specified in figures legends at day 1, 3, 5, 8 and sacrificed at day 9: 100 ng of IL-12 (R&D), IL-18 (R&D), IL-33 (Biolegend), IFNγ (Biolegend) or 20 µg of NMU (US Biological) per mouse and per instillation. For the Seahorse assays we elicited ILC2 with 0.5 mg IL-33, three doses i.p. over 10 days. Sorted ILC2 from lung were then cultured in presence of IL-7 and IL-2 (50ng/ml) for 7 days before addition of DMOG.

Flow cytometry

To identify mouse ILCs, single-cell suspensions were stained with mAb for known lineages and with mAb discriminating ILC subsets. mAbs for known lineages included CD3 (17A2, Biolegend), CD4 (RM4-5, Biolegend), CD8a (53-6.7, Biolegend), TCRαβ (H57-597, Biolegend), TCRγδ, (GL3, Biolegend) CD11b (M1/70, Biolegend), CD11c (N418, Biolegend), F4/80 (BM8, Biolegend), Ly6G (1A8, Biolegend), TER119 (TER-119, Biolegend), FcεRIa (MAR-1, Biolegend), CD19 (1D3/CD19, Biolegend), B220 (RA3-6B2, Biolegend), and CD49b (DX5, Biolegend). mAbs discriminating ILC subsets included CD45.2 (104, BD), CD90.2 (30-H12, Biolegend), CD127 (A7R34, eBioscience), NK1.1 (PK136, BD Biosciences), IL-18Rα (P3TUNYA, eBioscience), ST2 (RMST2-2, eBioscience), CD226 (10E5, Biolegend), CD49a (Ha31/8), NKp46 (29A1.4), KLRG1 (2F1, eBiosciences), and ICOS (C398.4A, Biolegend).
mAbs for intracellular staining included GATA3 (L50-823, BD Biosciences), T-bet (4B10, eBiosciences), RORγt (Q31-378, BD Biosciences), PLZF (9E12, Biolegend), TCF-1 (S33-966, BD), Arg1 (A1exF5, BD Biosciences), Ki-67 (SolA15, eBiosciences), Eomes (Dan11mag, eBiosciences, and HIF1α (D1S7W, Cell Signaling). After extracellular staining, cells were fixed and permeabilized (Foxp3 staining kit, eBiosciences) for intracellular staining. Samples from Biosafety Level 3 were inactivated for 2 hours at RT with 4% paraformaldehyde (ThermoFisher Scientific) after extracellular and intracellular staining.

Live/Dead fixable blue (eBiosciences) and mouse FcBlock (BD Biosciences) were used for all flow cytometry experiments. Cell staining was analyzed using LSR Fortessa flow cytometers (BD) and FlowJo software (v10). Cells were first gated in singlets (FSC-H vs. FSC-W and SSC-H vs. SSC-W) and live cells before further analyses.

Intracellular cytokines staining

For intracellular cytokines staining of ILCs, single-cell suspensions from lung were incubated at 37°C with Brefeldin A in association or not with PMA (50 ng/ml, Sigma)/Ionomycine (500 ng/ml, Sigma) or 50 ng/ml of IL-12 and IL-18 for 4 hours before being surface stained, fixed and permeabilized (Foxp3 staining kit, eBiosciences). mAbs for cytokines staining included IFN-γ (XMG1.2, Biolegend), IL-17A (TC11-18H10, BD Biosciences), IL-5 (TRFK5, BD Biosciences), and IL-13 (eBio13A, eBiosciences) To block glycolysis during *ex vivo* stimulation, cells were incubated in the presence of 10mM 2-DG (Sigma). *Mtb was* inactivated by incubation in PFA 4% for 2 hours at room temperature. For analyses of mitochondrial markers, cells were stained with MitoSOX Red (5 µM, eBiosciences) at 37°C for 30min.

Detection of mRNA using PrimeFlow

For PrimeFlow (ThermoFisher Scientific) experiments, single cell suspensions of lungs were analyzed for mRNA expression after extracellular/intracellular staining using the PrimeFlow RNA assay (eBioscience) and standard mouse probe sets for *Ifng*, *Il5,* and *Hif1a,* according to manufacturer's instructions for 96-well-plate staining.

ILC enrichment and cell-sorting

Lung ILCs were enriched from lung single-cell suspensions by using the EasySep™ Mouse ILC2 Enrichment Kit (StemCell). After enrichment, cells were stained with lineage mAb (CD3, CD4, CD8a, TCRαβ, TCRγδ, CD19, B220, CD11b, CD11c, F4/80, TER119, FcεRIa, CD49b, Ly6G) and ILC markers (CD90.2, CD45.2, NK1.1, ST2, IL-18Rα, CD49a). ILC2 were purified as $Lin^{-}CD45.2^{+}CD90.2^{+}NK1.1^{-}ST2^{+}$. ILC1-like were

549 purified as Lin$^-$CD45.2$^+$CD90.2$^+$NK1.1$^-$ST2$^+$CD49a$^+$IL-18Rα$^+$. Cells were sorted using a
550 FACSAria Fusion cytometer (BD, France).
551
552 ***In vitro* culture of ILC2**
553
554 Cell sorted ILC2 were incubated in 6-well plates at a density of 300,000 cells per ml
555 for 4 days with IL-2 (25 ng/ml, R&D) and IL-7 (25 ng/ml, R&D) in RPMI (Difco)
556 supplemented with 10 % FBS. After 4 days of culture, ILC2 were harvested for adoptive
557 transfer or incubated with DMOG (Sigma). For DMOG experiment, half of the medium
558 was removed and replaced with fresh medium containing IL-2 (25 ng/ml) and IL-7 (25
559 ng/ml) with or without DMOG (500 µg/ml) for 3 more days. Cell sorted ILC2 were
560 incubated in 6-well plates at a density of 300,000 cells per ml for 4 days with IL-2 (25
561 ng/ml, R&D) and IL-7 (25 ng/ml, R&D) in RPMI (Difco) supplemented with 10 % FBS.
562 After 4 days of culture, ILC2 were harvested for adoptive transfer or incubated with
563 DMOG (Sigma). For DMOG experiment, half of the medium was removed and
564 replaced with fresh medium containing IL-2 (25 ng/ml) and IL-7 (25 ng/ml) with or
565 without DMOG (500 µg/ml) for 3 more days. For the Seahorse assays, sorted ILC2
566 from lung were cultured in presence of IL-7 and IL-2 (50ng/ml) for 7 days before
567 addition of DMOG.
568
569
570 **SCENITH assay**
571
572 SCENITH experiments were performed as previously described[28] using the SCENITH
573 kit containing all reagents and anti-puromycin antibodies (requested from
574 www.scenith.com/try-it). Briefly, lung cell suspensions were stimulated for 15 minutes
575 at 37°C in the presence of the indicated inhibitors of various metabolic pathways then
576 incubated for 30 minutes with puromycin at 37°C. At the end of the incubation,
577 puromycin was stained with fluorescent anti-puromycin antibodies (Clone R4743L-E8)
578 by flow cytometry and the impact of the various metabolic inhibitors was quantitated
579 as described[28].
580
581 **Seahorse experiments**
582

583 1.5 to 2 x10^5 FACS sorted lung ILC2s per well were rested in a 96-well plate in
584 Glutamax RPMI (supplemented with 10% fetal bovine serum, non-essential amino
585 acids, 1 mM sodium pyruvate, 85 µM 2-mercapto-ethanol and 100 U/ml penicillin-
586 streptomycin) containing 25 ng/ml IL-7. After 24h cells were split and rested in fresh
587 IL-7 containing media for another 3 days. Subsequently, cells were cultured in fresh
588 medium containing 25 ng/ml IL-7 and 20 ng/ml of IL-2 in the presence or absence of
589 0.5 mM DMOG for a further 72 hours. To prepare for extracellular flux analysis cells
590 were then washed thoroughly in XF medium (modified DMEM) and adhered to the
591 Seahorse plate using 22.4 µg/ml Cell-Tak (Corning).

592 For glycolytic stress test, cells were plated at a density of 2x10^5 cells/well in XF medium
593 supplemented with 2 mM glutamine. Cells were incubated for 30-60 min at 37°C and
594 ECAR was measured under basal conditions, and in response to 10 mM glucose, 2
595 µM oligomycin and 50 mM 2-DG. For the mitochondrial stress test, cells were plated
596 at a density of 1.5x10^5 cells/well in XF medium supplemented with 2 mM glutamine, 1
597 mM sodium pyruvate and 25 mM glucose. Cells were incubated for 30-60 min at 37°C.
598 OCAR was measured under basal conditions, after injection of 2 µM oligomycin, 1.5
599 µM FCCP and 100 nM rotenone + 1 µM antimycin A. Extracellular flux assays were
600 done using a 96-well extracellular flux analyzer XFe-96 (Seahorse Bioscience).

601 Normalization by protein was used to correct for potential differences in seeding
602 densities across wells. Protein measurement was performed using the Pierce BCA
603 protein assay according to the manufacturer instructions.

604 **Quantification of cytokine production by ELISA**

605

606 Secreted cytokines from *Mtb*-infected lung supernatant were measured by ELISA
607 assays using kits from BD Bioscience (IFN-γ), according to the manufacturer's
608 instructions.

609

610 ***In vitro* differentiation of ILC2P**

611

612 To induce the ILC2 differentiation *in vitro*, bone marrow cells (BM) were collected from
613 hips, femurs and tibias. ILC2P were FACS-sorted from magnetically-enriched Sca$^+$
614 cells (Lin$^-$, Sca1$^+$ ckit dull, CD127$^+$, CD25$^+$). Purified ILC2P were cultured for 7 days in

aMEM complete medium (10% heat-inactivated FCS, 1% penicillin-streptomycin, 50 µM β-mercaptoethanol) on OP9-DL1, with 10 ng/ml of IL-7 and 10 ng/ml of SCF. In addition, depending on the experimental condition mouse IL-33 (10 ng/ml), mouse IL-12 (10 ng/ml), mouse IL-18 (10 ng/ml), mouse IFN-γ (10 ng/ml) have been added.

Quantitative RT-PCR analysis of transcripts

RNA from lungs homogenates was extracted using TRIzol reagent (Ambion) and RNeasy spin columns according to manufacturer's instructions (RNeasy kit, Qiagen). RNA was reverse transcribed into cDNA using M-MLV Reverse transcriptase (Invitrogen). RT-qPCR was performed using gene-targeted primers (Supplementary Table 1) as described above. Values were normalized using the housekeeping beta-actin gene (*Actb*) and expressed as a fold change. RNA from ILC2 culture were extracted using RLT (Qiagen) and RNA were reverse transcribed as previously described [41].

Statistical analyses

Statistical analyses were performed using GraphPad Prism 9 software. Agostino and Pearson normality tests were performed to determine whether data followed a normal distribution. Unpaired *t*-test (for normal data) or Mann-Whitney (for non-normal data) were performed when two samples were compared; ANOVA (for normal data) or Kruskal-Wallis (for non-normal data) tests were performed when more than two samples were compared. For all analyses, * indicates $P < 0.05$, ** indicates $P < 0.01$, *** indicates $P < 0.001$, and **** indicates $P < 0.0001$.

Acknowledgements

We acknowledge Emmanuelle Näser (TRI-IPBS platform, Toulouse) for flow cytometry and imagery analyses, Flavie Moreau, Céline Berrone and Aline Tridon (Anexplo-IPBS platform, Toulouse), and Sylvie Appolinaire and Celine Berraud (CREFRE animal facility, Toulouse) for mouse care and maintenance in conventional and BSL3 facilities. We thank Anne Dejean (CPTP, INSERM, Toulouse) for the kind gift of *Tbx21*$^{fl/fl}$ mice, Etienne Meunier (IPBS, CNRS, Toulouse) for the kind gift of *Stat1*$^{-}$

$^{-/-}$ mice and Richard Locksley (USCF, San Francisco) for the kind gift of Red5 mice. We thank Juan Carlos Zúñiga-Pflücker, University of Toronto for the kind gift of OP9-DL1 cells. We thank Geanncarlo Lugo-Villarino, Pauline Schmitt (IPBS, Toulouse), Sophie Laffont (CPTP, Toulouse) and Andrea Pichler (CRCT, Toulouse) for helpful discussion. This work was supported by Centre de la Recherche Scientifique (CNRS), the University of Toulouse, University Toulouse-III, Paul Sabatier, the French Ministry of Higher Education, Research and Innovation (Fellowship to D.C.), the Fondation pour la Recherche Médicale (DEQ20160334902 to ON), the Bettencourt Schueller Foundation (Grants Coup d'Élan pour la recherche française and Explore-TB to ON), MSDAVENIR (Grant Fight-TB to ON), the Agence Nationale de la Recherche (ANR-18-CE15-0004-01 to DH and ANR-11-EQUIPEX-0003 to ON), and the European Commission (TBVAC2020 n°643381 to ON). MRH is supported by a Royal Society and Wellcome Trust Sir Henry Dale Fellowship (105644/Z/14/Z), a Lister Institute of Preventative Medicine Prize and a BBSRC Project Grant (BB/T014482/1). The funders had no role in study design, data collection, and analysis, decision to publish, or preparation of the manuscript. This manuscript was edited at Life Science Editors.

Author contributions

D.C. and D.H. conceived and designed the study with input from O.N. ; D.C., A.C., M.Z.K., E.B., and F.L. performed the experiments ; E.L., J-P.G., and R.J.A contributed critical reagents and methods, D.C., G.E., J-C.G., R.J.A., M.R.H. and D.H. analyzed and interpreted the data; J-C.G., G.E., M.R.H., and Y.P., also provide important discussion for the project and critical feedback on the manuscript ; D.C., O.N. and D.H. wrote the manuscript. All coauthors read, reviewed and approved the manuscript.

Competing interests

The authors declare no competing interests

References

1. Meininger, I. *et al.* Tissue-Specific Features of Innate Lymphoid Cells. *Trends Immunol.* **41**, 902–917 (2020).
2. Vivier, E. *et al.* Innate Lymphoid Cells: 10 Years On. *Cell* **174**, 1054–1066 (2018).
3. Shih, H.-Y. *et al.* Developmental Acquisition of Regulomes Underlies Innate Lymphoid Cell Functionality. *Cell* **165**, 1120–1133 (2016).
4. Ricardo-Gonzalez, R. R. *et al.* Tissue signals imprint ILC2 identity with anticipatory function. *Nat. Immunol.* **19**, 1093–1099 (2018).
5. Shi, L. *et al.* Infection with Mycobacterium tuberculosis induces the Warburg effect in mouse lungs. *Sci. Rep.* **5**, 1–13 (2015).
6. Fernández-García, M. *et al.* Comprehensive Examination of the Mouse Lung Metabolome Following Mycobacterium tuberculosis Infection Using a Multiplatform Mass Spectrometry Approach. *J. Proteome Res.* **19**, 2053–2070 (2020).
7. Svedberg, F. R. *et al.* The lung environment controls alveolar macrophage metabolism and responsiveness in type 2 inflammation. *Nat. Immunol.* **20**, 571–580 (2019).
8. Saluzzo, S. *et al.* First-Breath-Induced Type 2 Pathways Shape the Lung Immune Environment. *Cell Rep.* **18**, 1893–1905 (2017).
9. O'Garra, A. *et al.* The Immune Response in Tuberculosis. *Annu. Rev. Immunol.* **31**, 475–527 (2013).
10. Orme, I. M., Roberts, A. D., Griffin, J. P. & Abrams, J. S. Cytokine secretion by CD4 T lymphocytes acquired in response to Mycobacterium tuberculosis infection. *J. Immunol.* **151**, 518–525 (1993).
11. Martínez-Barricarte, R. *et al.* Human IFN-γ immunity to mycobacteria is governed by both IL-12 and IL-23. *Sci. Immunol.* **3**, (2018).
12. Urdahl, K., Shafiani, S. & Ernst, J. Initiation and regulation of T-cell responses in tuberculosis. *Mucosal Immunol.* **4**, 288–293 (2011).
13. Bal, S. M., Golebski, K. & Spits, H. Plasticity of innate lymphoid cell subsets. *Nat. Rev. Immunol.* 1–14 (2020) doi:10.1038/s41577-020-0282-9.
14. Silver, J. S. *et al.* Inflammatory triggers associated with exacerbations of COPD orchestrate plasticity of group 2 innate lymphoid cells in the lungs. *Nat. Immunol.* **17**, 626–635 (2016).

15. Nussbaum, J. C. *et al.* Type 2 innate lymphoid cells control eosinophil homeostasis. *Nature* **502**, 245–248 (2013).

16. Ghaedi, M. *et al.* Single-cell analysis of RORα tracer mouse lung reveals ILC progenitors and effector ILC2 subsets. *J. Exp. Med.* **217**, (2020).

17. Zeis, P. *et al.* In Situ Maturation and Tissue Adaptation of Type 2 Innate Lymphoid Cell Progenitors. *Immunity* **53**, 775-792.e9 (2020).

18. Weizman, O.-E. *et al.* ILC1 Confer Early Host Protection at Initial Sites of Viral Infection. *Cell* **171**, 795-808.e12 (2017).

19. Chiossone, L., Dumas, P.-Y., Vienne, M. & Vivier, E. Natural killer cells and other innate lymphoid cells in cancer. *Nat. Rev. Immunol.* **18**, 671–688 (2018).

20. Kinjo, Y. *et al.* Contribution of IL-18 to Th1 response and host defense against infection by Mycobacterium tuberculosis: a comparative study with IL-12p40. *J. Immunol. Baltim. Md 1950* **169**, 323–329 (2002).

21. Duerr, C. U. *et al.* Type I interferon restricts type 2 immunopathology through the regulation of group 2 innate lymphoid cells. *Nat. Immunol.* **17**, 65–75 (2016).

22. Moro, K. *et al.* Interferon and IL-27 antagonize the function of group 2 innate lymphoid cells and type 2 innate immune responses. *Nat. Immunol.* **17**, 76–86 (2016).

23. Cardoso, V. *et al.* Neuronal regulation of type 2 innate lymphoid cells via neuromedin U. *Nature* **549**, 277–281 (2017).

24. Klose, C. S. N. *et al.* Differentiation of Type 1 ILCs from a Common Progenitor to All Helper-like Innate Lymphoid Cell Lineages. *Cell* **157**, 340–356 (2014).

25. Wallrapp, A. *et al.* The neuropeptide NMU amplifies ILC2-driven allergic lung inflammation. *Nature* **549**, 351–356 (2017).

26. Joseph, A. M., Monticelli, L. A. & Sonnenberg, G. F. Metabolic regulation of innate and adaptive lymphocyte effector responses. *Immunol. Rev.* **286**, 137–147 (2018).

27. Monticelli, L. A. *et al.* Arginase 1 is an innate lymphoid-cell-intrinsic metabolic checkpoint controlling type 2 inflammation. *Nat. Immunol.* **17**, 656–665 (2016).

28. Argüello, R. J. *et al.* SCENITH: A Flow Cytometry-Based Method to Functionally Profile Energy Metabolism with Single-Cell Resolution. *Cell Metab.* **32**, 1063-1075.e7 (2020).

29. Heiden, M. G. V., Cantley, L. C. & Thompson, C. B. Understanding the Warburg Effect: The Metabolic Requirements of Cell Proliferation. *Science* **324**, 1029–1033 (2009).

745 30. Palazon, A., Goldrath, A. W., Nizet, V. & Johnson, R. S. HIF Transcription
746 Factors, Inflammation, and Immunity. *Immunity* **41**, 518–528 (2014).
747 31. Li, Q. *et al.* E3 Ligase VHL Promotes Group 2 Innate Lymphoid Cell Maturation
748 and Function via Glycolysis Inhibition and Induction of Interleukin-33 Receptor.
749 *Immunity* **48**, 258-270.e5 (2018).
750 32. Muri, J. & Kopf, M. Redox regulation of immunometabolism. *Nat. Rev. Immunol.*
751 1–19 (2020) doi:10.1038/s41577-020-00478-8.
752 33. Perdomo, C. *et al.* Mucosal BCG Vaccination Induces Protective Lung-Resident
753 Memory T Cell Populations against Tuberculosis. *mBio* **7**, (2016).
754 34. Ardain, A. *et al.* Group 3 innate lymphoid cells mediate early protective immunity
755 against tuberculosis. *Nature* **570**, 528–532 (2019).
756 35. Stehle, C., Hernández, D. C. & Romagnani, C. Innate lymphoid cells in lung
757 infection and immunity. *Immunol. Rev.* **286**, 102–119 (2018).
758 36. Lim, A. I. *et al.* Systemic Human ILC Precursors Provide a Substrate for Tissue
759 ILC Differentiation. *Cell* **168**, 1086-1100.e10 (2017).
760 37. Lim, A. I. & Di Santo, J. P. ILC-poiesis: Ensuring tissue ILC differentiation at the
761 right place and time. *Eur. J. Immunol.* **49**, 11–18 (2019).
762 38. Bando, J. K., Nussbaum, J. C., Liang, H.-E. & Locksley, R. M. Type 2 innate
763 lymphoid cells constitutively express arginase-I in the naïve and inflamed lung. *J.*
764 *Leukoc. Biol.* **94**, 877–884 (2013).
765 39. Peng, M. *et al.* Aerobic glycolysis promotes T helper 1 cell differentiation through
766 an epigenetic mechanism. *Science* **354**, 481–484 (2016).
767 40. Chang, C.-H. *et al.* Posttranscriptional Control of T Cell Effector Function by
768 Aerobic Glycolysis. *Cell* **153**, 1239–1251 (2013).
769 41. Troegeler, A. *et al.* C-type lectin receptor DCIR modulates immunity to
770 tuberculosis by sustaining type I interferon signaling in dendritic cells. *Proc. Natl. Acad.*
771 *Sci. U. S. A.* **114**, E540–E549 (2017).
772

Figure 1

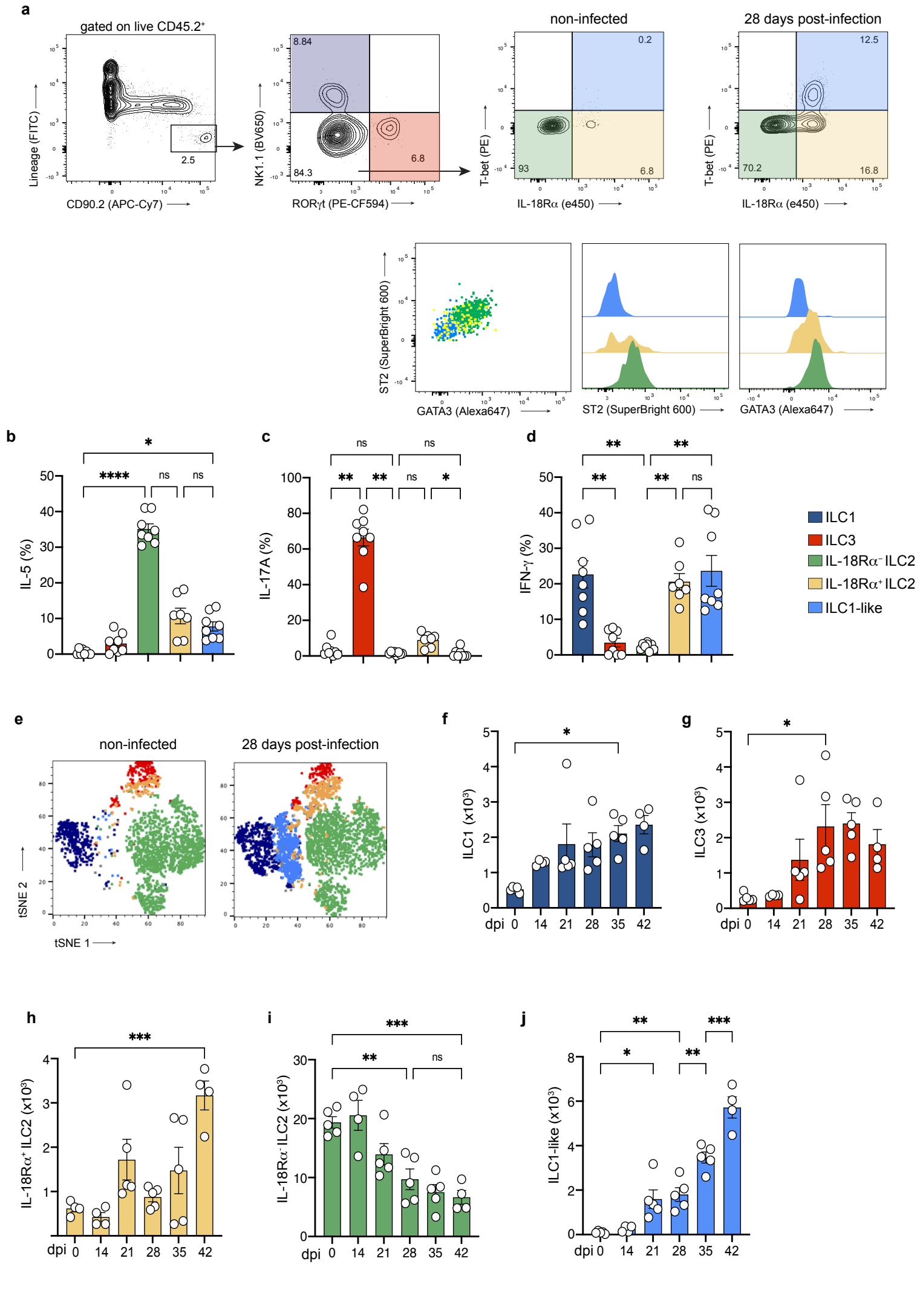

Figure 1. IFN-γ**-producing ILC1-like cells emerge during *Mtb* infection. (a)** Representative dot plots showing the gating strategy used to analyze ILC subsets in the lungs of C57BL/6 mice after doublets exclusion (top graphs): ILC1 (dark blue), ILC3 (red), IL-18Rα$^-$ ILC2 (green), IL-18Rα$^+$ ILC2 (yellow) and T-bet$^+$IL-18Rα$^+$ ILC (light blue) are depicted in non-infected and *Mtb*-infected mice. Representative expression of GATA3 and ST2 on the indicated ILC subsets following the above color code) (bottom graphs). **(b-d)** Percentage of IL-5 (b), IL-17A (c), and IFN-γ (d) in the indicated ILC subsets at day 28 post-infection in C57BL/6 mice. **(e)** Unsupervised t-SNE distribution of total lung Lin$^-$CD90.2$^+$ populations at steady-state (left graph) and during *Mtb* infection (right graph). Based on gating strategy defined in Fig.1a, ILC subsets were depicted with the same color code: ILC1 in dark blue, ILC3 in red, IL-18Rα$^-$ ILC2 in green, IL-18Rα$^+$ ILC2 in yellow and ILC1-like cells (light blue). **(f-j)** Absolute numbers of ILC1 (f), ILC3 (g), IL-18Rα$^+$ ILC2 (h), IL-18Rα$^-$ ILC2 (i), and ILC1-like cells (j) at the indicated days after *Mtb* infection. Prior to sacrifice, mice were injected with fluorescent anti-CD45.2 to distinguish vascular and parenchymal cells. ILC1, ILC3, IL-18Rα$^-$ ILC2 and IL-18Rα$^+$ ILC2 have been gated on lung-resident cells. In **(b-d, f-j)**, data are representative of five independent experiments with each symbol representing an individual mouse, graphs depict data as mean (± s.e.m) and statistical analysis was performed using two-way ANOVA (*, $p<0.05$; **, $P<0.01$; ***, $p<0.001$; ****, $p<0.0001$).

Figure 2

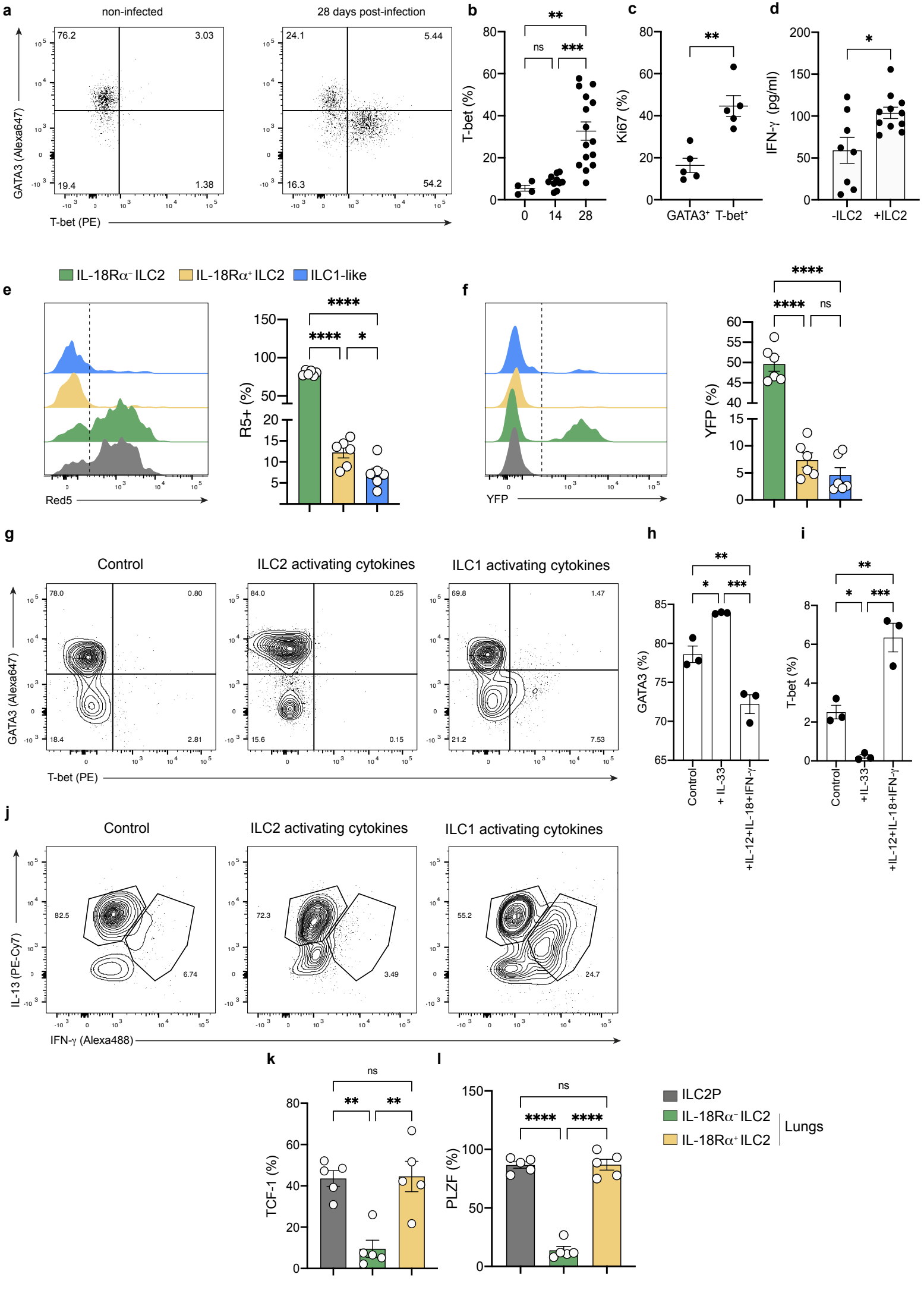

Figure 2. ILC2 give rise to ILC1-like cells during *Mtb* infection. (a) A representative dot-plot of GATA3 and T-bet expression in Lin$^-$CD45.2$^-$CD90.2$^-$ cells isolated from *Rag2*$^{-/-}$*Il2rg*$^{-/-}$ mice adoptively transferred with purified ILC2 then left uninfected (right) or infected with *Mtb* (left). **(b)** Percentages of T-bet expressing ILC at different days post-infection. **(c)** Percentages of Ki67$^+$ cells among GATA3^{hi}T-bet^{low} and GATA3^{low}T-bet^{hi} cells. **(d)** Concentration of IFN-γ determined by ELISA in total lungs from *Mtb*-infected *Rag2*$^{-/-}$*Il2rg*$^{-/-}$ mice transferred (+ILC2) or not (-ILC2) with purified ILC2, the ELISA results were pooled from two independent experiments. **(e-f)** Representative histograms showing IL-5 (e) and YFP (f) expression among IL-18Rα$^-$ ILC2 (green), IL-18Rα$^+$ ILC2 (yellow), and ILC1-like (blue) in non-infected *vs*. *Mtb*-infected IL-5^{Cre}ROSA26^{YFP} mice. Grey histograms represent IL-5 (e) or YFP (f) expression in IL-18Rα$^-$ ILC2 in IL-5^{Cre} mice. Vertical dotted line indicates the threshold determining positivity. Bar graphs show percentages of IL-5 (e) or YFP (f) cells in IL-18Rα$^-$ ILC2 (green), IL-18Rα$^+$ ILC2 (yellow), and ILC1-like (blue) at day 28 post-infection in IL-5^{Cre}ROSA26^{YFP}. **(g)** Representative dot-plot showing GATA3 and T-bet expression in bone marrow ILCP in an *in vitro* differentiation assay performed in control conditions or in the presence of ILC2 or ILC1 activating cyokines. **(h-i)** Expression of GATA3 **(h)** and T-bet **(i)** in bone marrow ILC2P after 7 days of culture with IL-7/SCF ± IL-33 ± IL-12/IL-18/IFN-γ . **(j)** Representative dot-plot showing IL-13 and IFN-γ expression in bone marrow ILC2P in an *in vitro* differentiation assay under the indicated conditions after *ex vivo* stimulation with PMA/ionomycin. (k-l) Percentage of TCF-1 **(k)** and PLZF **(l)** in ILC2P from bone marrow (grey) compared to IL-18Rα$^-$ ILC2 (green) and IL-18Rα$^+$ ILC2 (yellow) from lungs of C57BL/6 mice at steady-state. Each symbol represents an individual mouse **(b, c, d, e, f, k, l)** or biological replicates (**h, i**). Statistical analysis was performed using Anova two-way **(b, e, f, h, i, k, l)** and Mann-Whitney test **(c, d)** (*, p<0.05; **, P<0.01; ***, p<0.001; ****, p<0.0001). Graphs depict data as mean (± s.e.m). Data are representative of three **(b, c)**, two **(g-l),** a pool of two **(d)** independent experiments and one experiment with 6 mice per group (e ,f).

Figure 3

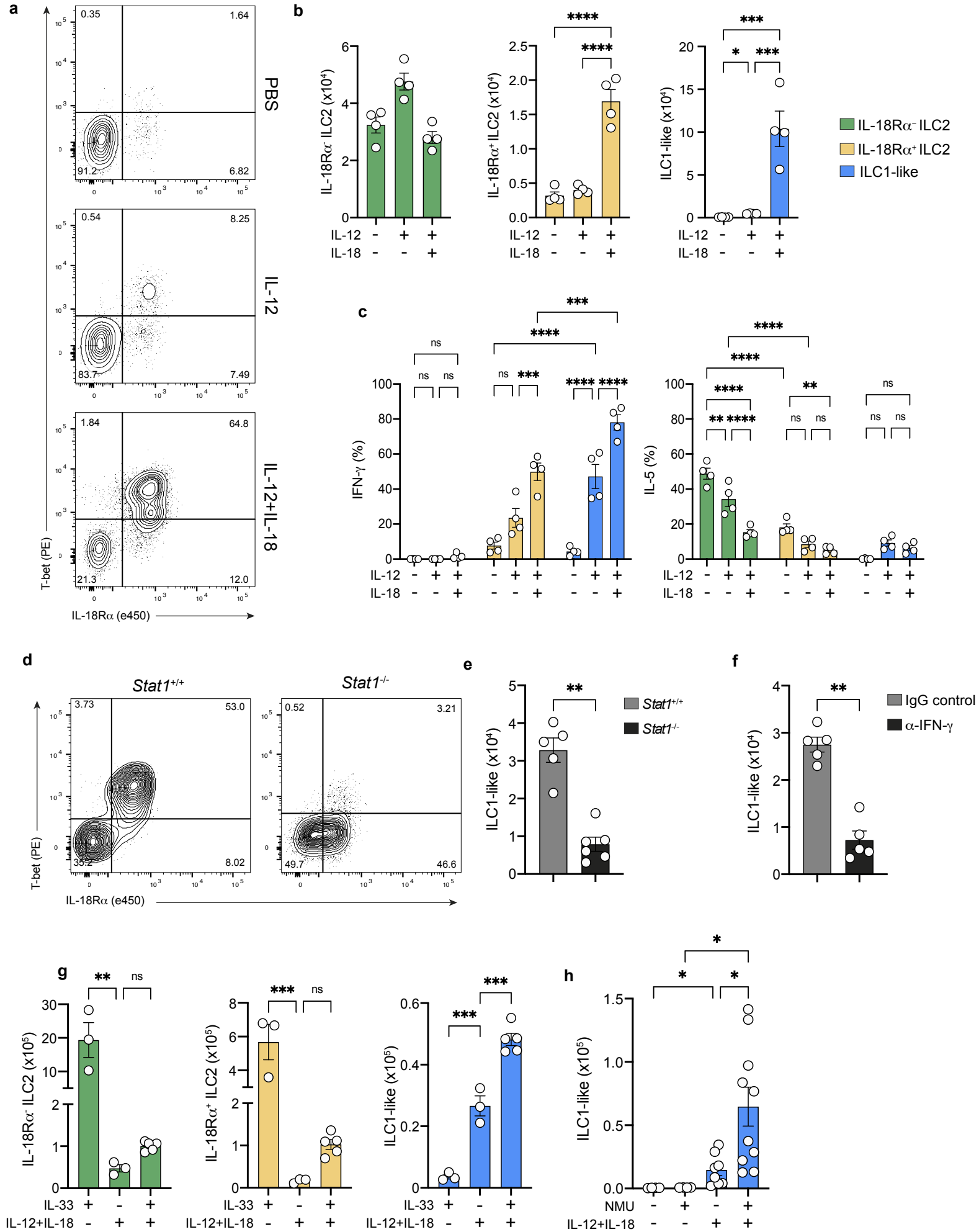

Figure 3. The inflammatory environment shapes the fate of immature ILC2. (a) Representative dot-plots of T-bet and IL18Rα expression after intranasal administration of PBS, IL-12, and IL-12+IL-18 in *Rag2*$^{-/-}$ mice. **(b)** Absolute numbers of IL-18Rα^{-} ILC2 (green), IL-18Rα^{+} ILC2 (yellow) and ILC1-like cells (blue) after cytokine treatment or control (PBS). **(c)** Percentages of cells expressing IFN-γ (left) or IL-5 (right) among the indicated ILC subsets after *ex vivo* stimulation with PMA/ionomycin in the presence of brefeldin A for 4h. **(d)** Representative dot-plot of T-bet and IL-18Rα expression in *Stat1*$^{+/+}$ *vs. Stat1*$^{-/-}$ mice after intranasal administration of IL-12 and IL-18. **(e)** Absolute numbers of ILC1-like cells in *Stat1*$^{+/+}$ *vs. Stat1*$^{-/-}$ mice treated as in **(a)**. **(f)** Absolute numbers of ILC1-like cells in in IL-12+IL-18 treated mice having received i.p injections of α-IFN-γ or control IgG. **(g)** Absolute numbers of IL-18Rα^{-} ILC2 (green), IL-18Rα^{+} ILC2 (yellow) and ILC1-like cells (blue) after intranasal administration of PBS (control), IL-12+IL-18, or IL-12+IL-18+IL-33. **(h)** Absolute numbers of ILC1-like cells after intranasal administration of PBS (control), neuromedin U (NMU), IL-12+IL-18, or IL-12+IL-18+NMU. In **(b, c, e-h),** each symbol represents an individual mouse. Statistical analysis was performed using Mann-Whitney (e, f) and two-way ANOVA **(b, c, g, and h)** tests (*, $p<0.05$; **, $P<0.01$; ***, $p<0.001$; ****, $p<0.0001$). Graphs depict data as mean (± s.e.m). Data are representative of three **(b-c, g)** and two **(d-f, h)** independent experiments.

Figure 4

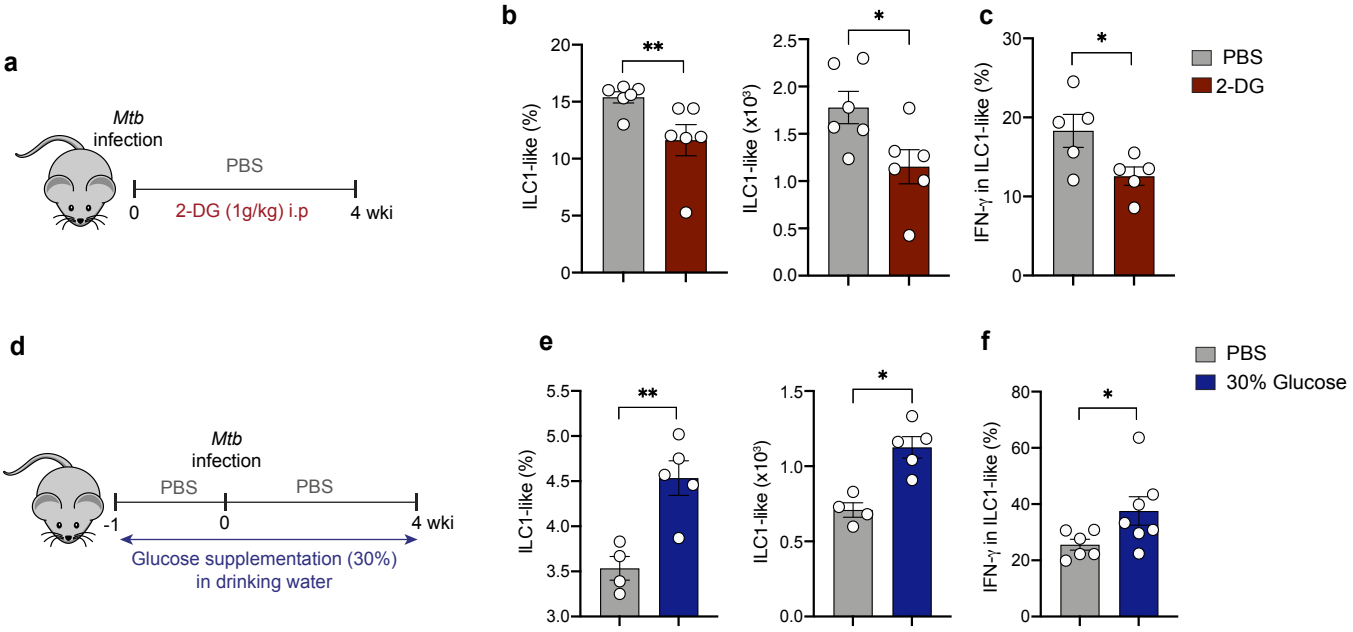

Figure 4. Metabolic environment dictates ILC2 plasticity through glucose availability. (a) Scheme of the experimental model for *in vivo* treatment with 2-DG. **(b)** Percentages (left) and absolute numbers (right) of ILC1-like cells in *Rag2*$^{-/-}$ mice treated or not with 2-DG during *Mtb* infection. Measurements were performed at day 28 post-infection. **(c)** Percentages of IFNγ-producing cells among ILC1-like cells after *ex vivo* stimulation with PMA/ionomycin in the presence of brefeldin A for 4h from PBS *vs.* 2-DG treated mice. **(d)** Scheme of the experimental model for *in vivo* glucose supplementation in drinking water. **(e)** As in **(b)** except that mice treated with 30% glucose in their drinking water. **(f)** As in **(c)** except that mice were treated or not with 30% glucose in their drinking water. In **(b, c, e, f)**, each symbol represents an individual mouse and statistical analysis was performed using Mann-Whitney (*, $p<0.05$; **, $P<0.01$; ***, $p<0.001$; ****, $p<0.0001$). Graphs depict data as mean (± s.e.m) from three **(b, c)** or two **(e, f)** independent experiments.

Figure 5

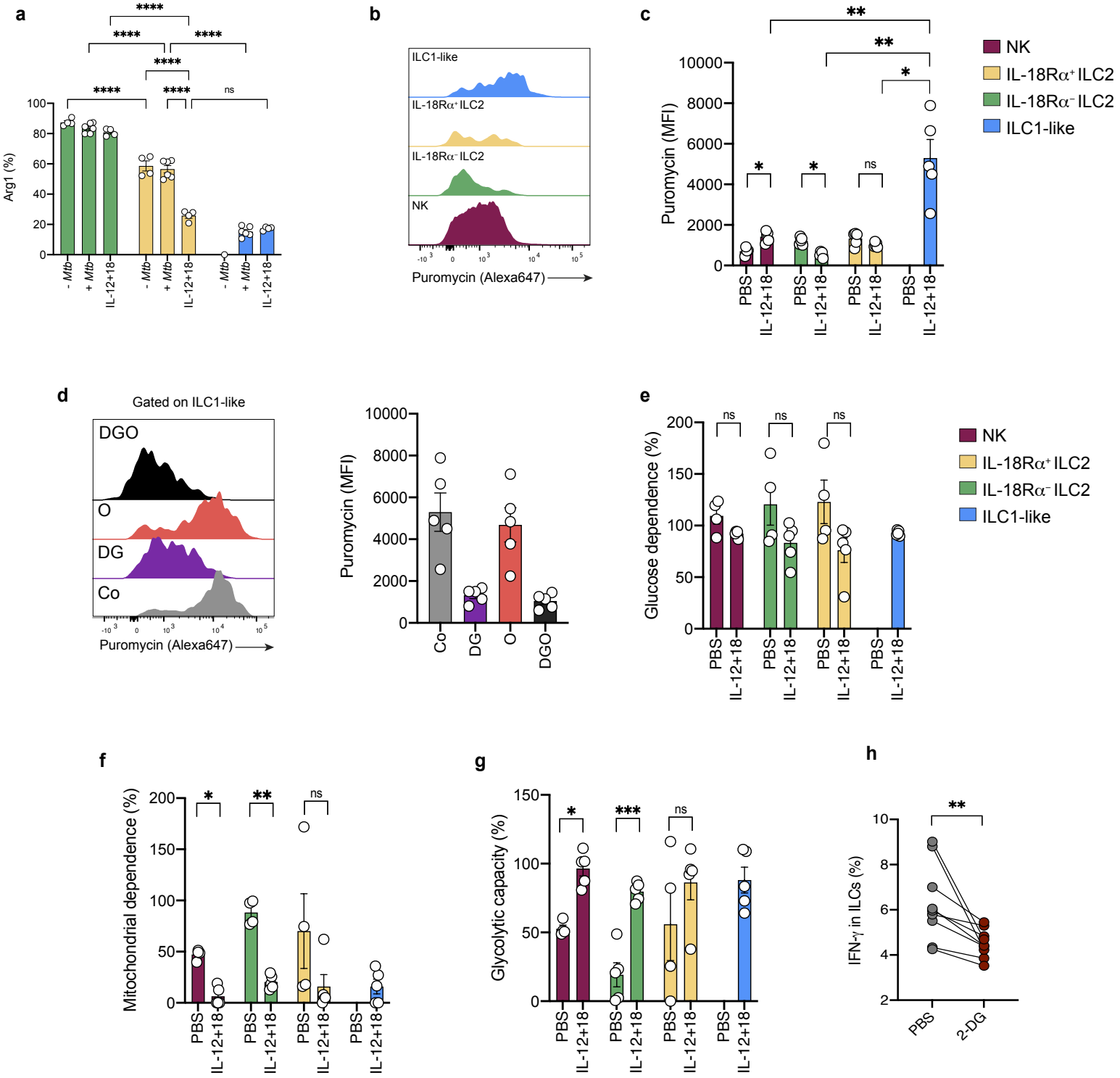

Figure 5. ILC1-like cells display a glycolytic dependence. (a) Percentages of Arg1$^+$ cells among IL-18Rα^- ILC2 (green), IL-18Rα^+ ILC2 (yellow), and ILC1-like cells (blue) defined at steady state (- *Mtb*), upon *Mtb* infection (+ *Mtb*) or intranasal administration of cytokines (IL-12+IL-18). **(b)** Representative histograms of puromycin staining in NK cells (violet), IL-18Rα ILC2$^-$ (green), IL-18Rα^+ ILC2 (yellow), and ILC1-like cells (blue) in IL-12+IL-18 treated mice. **(c)** Expression of puromycin (MFI) in NK cells (violet), IL-18Rα^- ILC2 (green), IL-18Rα^+ ILC2 (yellow), and ILC1-like cells (blue) in PBS *vs.* IL-12+IL-18 treated mice. **(d)** Representative histograms of puromycin staining (left) and quantification (MFI, right) in ILC1-like cells from IL-12+IL-18 treated mice after incubation with various metabolic inhibitors (Co, control; DG, 2-Deoxyglycose; O, oligomycin; DGO, 2-Deoxyglucose + Oligomycin). **(e-g)** Percentage of glucose dependence **(e)**, mitochondrial dependence **(f)**, and glycolytic capacity **(g)** in NK (violet), IL-18Rα^- ILC2 (green), IL-18Rα^+ ILC2 (yellow), and ILC1-like cells (blue) in PBS *vs.* IL-12+IL-18 treated mice. **(h)** Expression of IFN-γ in total ILCs after *ex vivo* stimulation with IL-12+IL-18 in the presence or absence of 2-DG. In **(a-h)**, graphs depict data as mean (± s.e.m) from two independent experiments, each symbol represents an individual mouse. Statistical analysis was performed using two-way ANOVA **(a, c, e, f, g)** or Wilcoxon **(h)** test (*, p<0.05; **, P<0.01; ***, p<0.001; ****, p<0.0001).

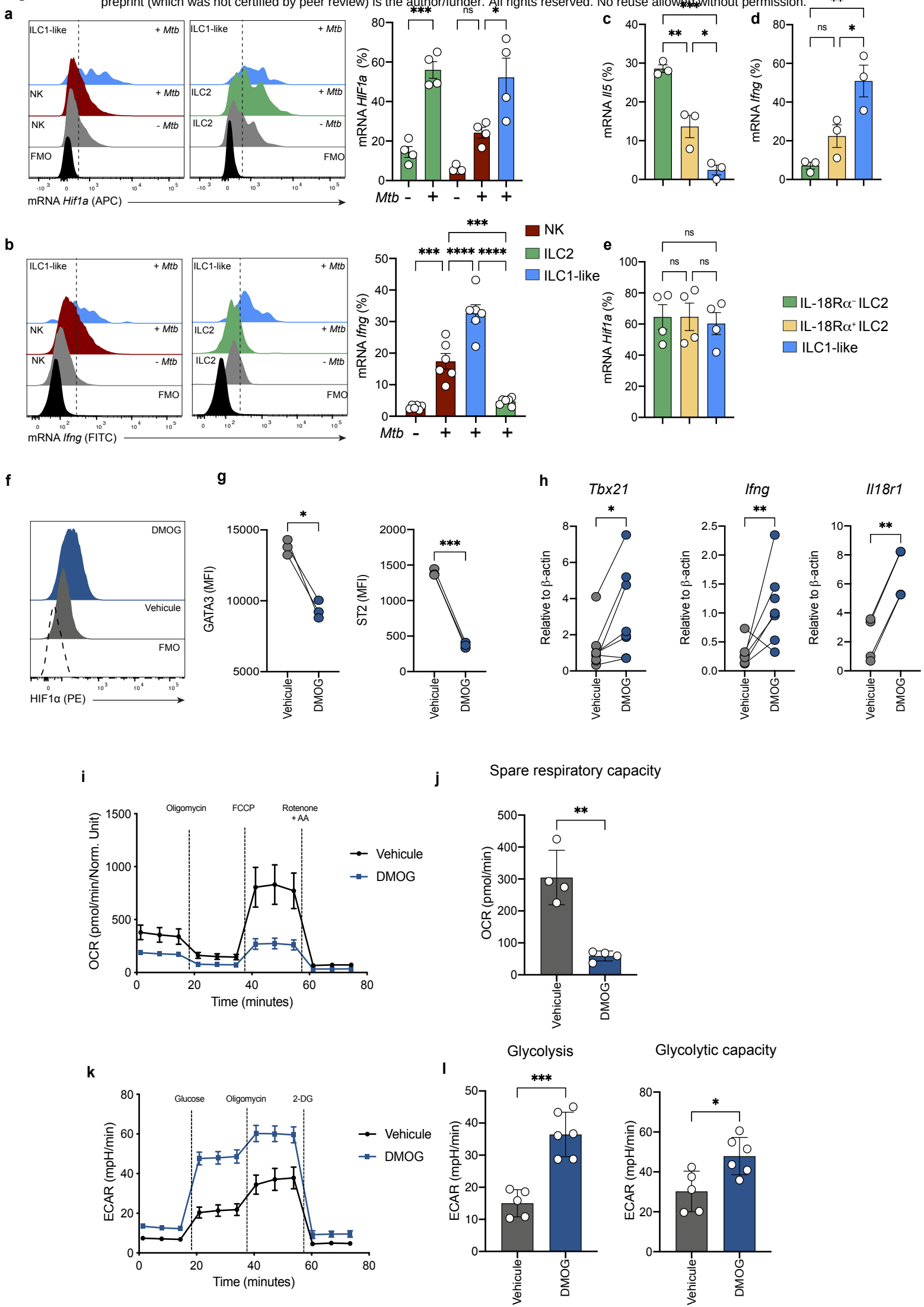

Figure 6. Metabolic reprogramming involving HIF1α controls ILC2 plasticity. (a) Representative histograms (left) and quantification (right) of *Hif1a* mRNA expression *via* prime-flow on NK cells (left) and ILC2 (middle) compared to ILC1-like cells in non-infected *vs. Mtb*-infected *Rag2*$^{-/-}$ mice (28 dpi). The dot line represents the positivity according to the fluorescence minus one (FMO). **(b)** As in **(a)** but for *Ifng* mRNA expression. **(c-e)** Percentages of the indicated IL-18Rα^{-} ILC2 (green), IL-18Rα^{+} ILC2 (yellow) and ILC1-like (blue) populations expressing *Il5* **(c)**, *Ifng* **(d)**, *Hif1a* **(e)** mRNA in *Mtb*-infected *Rag2*$^{-/-}$ mice (28 dpi). **(f)** Histograms showing HIF1α protein expression in ILC2 cultured in the absence (vehicle, grey) or presence of DMOG (blue). The dot line represents FMO for HIF1α detection. **(g)** Quantitative analysis of the intensity of GATA3 (left) and ST2 (right) expression in ILC2 cultured in the absence (vehicle) or presence of DMOG. **(h)** as in **(g)** except that the expression of *Tbx21*, *Ifng* and *Il18ra1* mRNA was analyzed by RT-qPCR. **(i, j)** Seahorse analysis of mitochondrial respiration (i) with quantification of spare respiratory capacity (j) in ILC2 cultured in the presence or absence of DMOG. **(k, l)** Seahorse analysis of glycolytic stress test (k) with quantitation of glycolysis and glycolytic capacity (**l**) of ILC2 cultured in the presence or absence of DMOG. Each symbol in **(a-e, g, h, j, and l)** represents an individual mouse. Statistical analysis was performed using two-ANOVA **(a-e),** and paired t test **(g-l)** (*, p<0.05; **, P<0.01; ***, p<0.001; ****, p<0.0001). Graphs depict data as mean (± s.e.m). Data are representative of three **(f)**, two **(a-e, g, i-l)**, a pool of three **(h)** independent experiments.

Figure 7

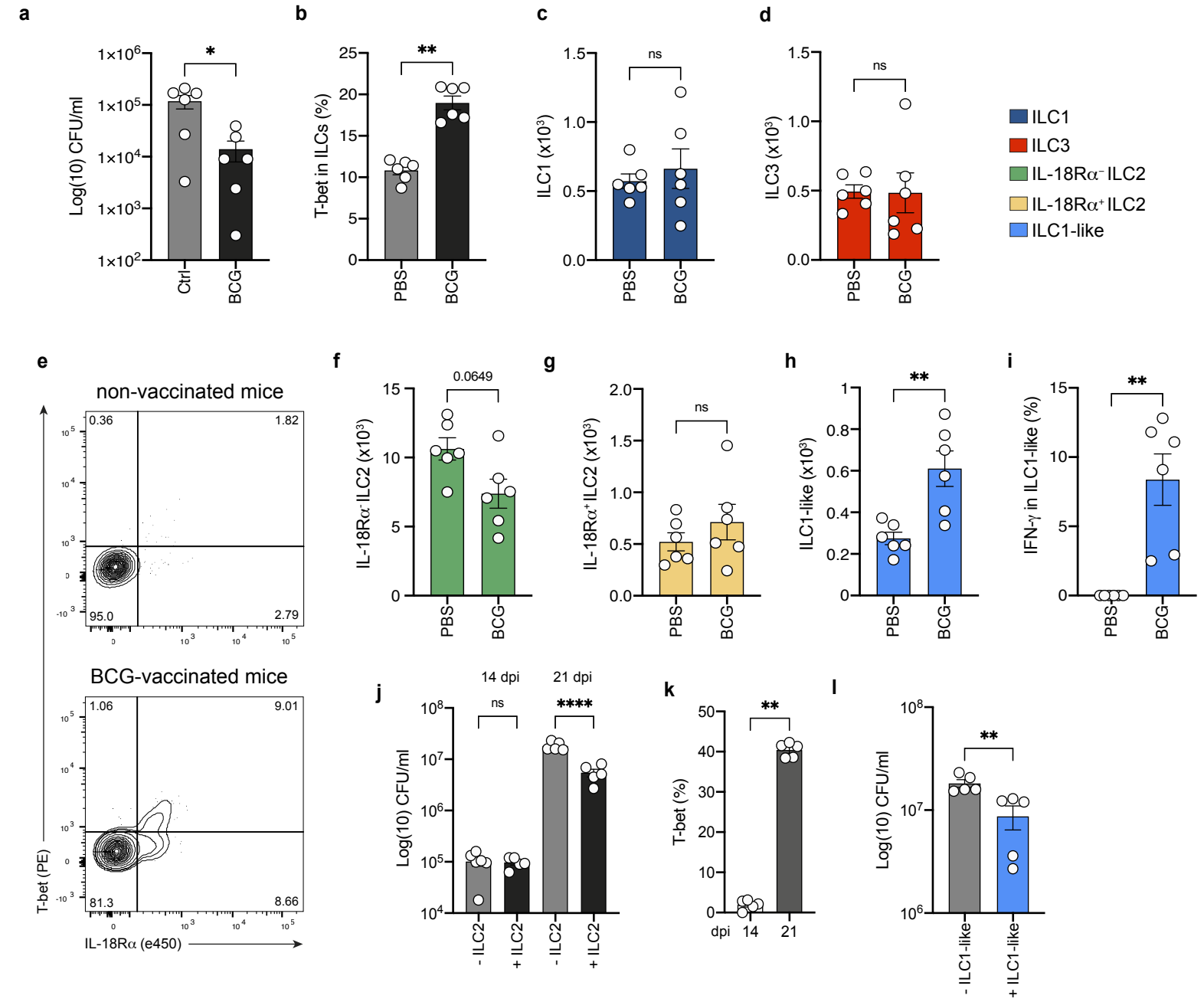

Figure 7. ILC1-like cells confer protection against *Mtb*. (a) Mycobacterial loads at day 14 post-infection in C57BL/6 mice vaccinated or not (PBS) with $1x10^5$ BCG via the intranasal route 60 days prior *Mtb* infection. **(b)** Percentages of total lung ILC expressing T-bet. **(c-d)** Absolute numbers of ILC1 **(c)** andILC3 **(d)** at day 14 post-infection in C57BL/6 mice vaccinated or not (PBS) with $1x10^5$ BCG via the intranasal route 60 days prior *Mtb* infection. **(e)** Representative dot-plots of T-bet and IL18Rα expression in *Mtb*-infected non-vaccinated (top) *vs.* BCG-vaccinated (bottom) mice at day 14 post-infection. **(f-h)** Absolute numbers of IL-18Rα^- ILC2 **(f)**, IL-18Rα^+ ILC2 **(g),** and ILC1-like cells **(h)** at day 14 post-infection in C57BL/6 mice vaccinated or not (PBS) with $1x10^5$ BCG via the intranasal route 60 days prior *Mtb* infection. **(i)** Percentage of IFN-γ^+ cells among ILC1-like cells in *Mtb*-infected unvaccinated *vs.* vaccinated mice after *ex vivo* stimulation with PMA/ionomycin in the presence of brefeldin A for 4h. **(j)** Mycobacterial loads at day 14 and 21 post-infection in *Rag2*$^{-/-}$ *Il2rg*$^{-/-}$ mice having received (+ILC2) or not (-ILC2) an adoptive transfer of sorted ILC2 cells one day before *Mtb* infection. **(k)** In the model presented in **(j)**, T-bet expression was analyzed in lung ILCs 14- or 21-days post *Mtb* infection. **(l)** Bacterial loads at day 21 post-infection in *Rag2*$^{-/-}$*Il2rg*$^{-/-}$ mice having received (+ILC1-like) or not (-ILC1like) an adoptive transfer of ILC1-like cells from IL-12+IL-18+IL-33 treated *Rag2*$^{-/-}$ mice one day before *Mtb* infection. Each symbol in **(a-d, f-l)** represents an individual mouse. Statistical analysis was performed using Mann-Whitney test **(a-d, f-i, k, l)** and two-way ANOVA **(j)** (*, p<0.05; **, P<0.01; ***, p<0.001; ****, p<0.0001). Graphs depict data as mean (± s.e.m). Data are representative of one **(a-i),** three **(j, k)** and two **(l)** independent experiments.